An integral approach to compute compressible fluid flows in domains containing obstacles

Jean-Marc Hérard, Xavier Martin

An integral approach to compute compressible fluid flows in domains containing obstacles

Jean-Marc Hérard[†]
[†] *EDF R&D,MFEE, 6 quai Watier, F78400, Chatou,*
I2M, UMR CNRS 7353, 39 rue Joliot Curie, F13453 Marseille.
jean-marc.herard@edf.fr

Xavier Martin[⋆]
[⋆] *EDF R&D,MFEE, 6 quai Watier, F78400, Chatou,*
I2M, UMR CNRS 7353, 39 rue Joliot Curie, F13453 Marseille.
xavier-x.martin@edf.fr

Abstract

We detail in this paper an integral approach in order to cope with the computation of flows of a compressible fluid in a physical domain containing many small obstacles. The basic methodology and the main ingredients used in schemes are provided, together with some exact solutions that are used to benchmark the integral approach. The latter is compared to the reference solution that accounts for all obstacles through standard wall-boundary conditions. Numerical results are also shown to be more accurate than the standard well-balanced approach. This work is actually the sequel of paper [1] that investigates the computation of compressible flows in variable cross-section ducts.

Key words : Finite volumes / Integral approach / Flows in obstructed media / Well-balanced approach / Entropy

1 Introduction

The main purpose in this paper is to provide some way to investigate fluid evolutions in a physical domain containing many tiny obstacles. The basic underlying idea is indeed very simple. Actually, in a preliminary work [1], classical one-dimensional well-balanced (WB) formulations of fluid flows in pipes with varying cross sections have been investigated in detail, and compared with an integral unsteady formulation that allows the computation of compressible flows, whatever the cross section is

(even discontinuous, or with a closed flow path). The comparison included several situations, and both the classical well-balanced formulation and the integral formulation were confronted to a reference solution that was obtained by computing the multidimensional model on a very fine mesh, and the geometrical representation of all obstacles. It occured that in all situations, the integral approach performs much better (when compared with the reference unsteady solution); in addition, the WB approach may crash when the ratio of neighbouring sections is too high. The work presented in this paper is in fact the sequel of this preliminary work.

When restricting to some specific communities, including at least the nuclear community ([4]), it must be first recalled that an entire generation of codes has been developed ([27, 31, 18]), that is grounded on the use of the so-called porous approach ([3, 7]). This one aimed at getting approximations of the main patterns of a single phase or two-phase flow in a physical domain where the fluid flows around many small obstacles. The basic idea was to use a set of PDE's that is commonly encountered when dealing with porous media. In that case, when neglecting viscous contributions, a toy model for compressible single phase flows is (see for instance [27]):

$$\left\{ \begin{array}{l} \dfrac{\partial \vartheta(\mathbf{x})\rho}{\partial t} + \nabla.(\vartheta(\mathbf{x})\underline{Q}) = 0 \\ \dfrac{\partial \vartheta(\mathbf{x})\underline{Q}}{\partial t} + \nabla.(\vartheta(\mathbf{x})\underline{Q} \otimes \underline{Q}/\rho) + \vartheta(\mathbf{x})\nabla P = \vartheta(\mathbf{x})\underline{S}_U \\ \dfrac{\partial \vartheta(\mathbf{x})E}{\partial t} + \nabla.\left(\vartheta(\mathbf{x})\underline{Q}(E+P)/\rho\right) = \vartheta(\mathbf{x})\underline{Q}.\underline{S}_U/\rho + \vartheta(\mathbf{x})S_E \end{array} \right. \tag{1}$$

where $\vartheta(\mathbf{x})$ stands for the ratio of the volume occupied by the fluid versus the total volume considered:

$$\vartheta(\mathbf{x}) = vol(\Omega^{fluid})/vol(\Omega)$$

Source terms $\underline{S}_U$ and S_E on the right hand side of (1) include gravity effects and regular head losses due to viscous contributions. Several schemes may be used in order to get approximate solutions of this set, when restricting to regular distributions for $\vartheta(\mathbf{x})$, for instance, those relying on the well-balanced scheme of J.M. Greenberg, L. Gosse and A.Y. Leroux introduced in the pioneering papers [19, 17] or other variants (see [16, 2, 26, 20, 25, 6] among many others). In addition, it was reported in [14] that the use of the WB approach is in fact mandatory when handling (1) with discontinuous cross sections; otherwise, some convergence towards some wrong solution may be obtained.

However, some situations exist where it becomes mandatory to handle sudden spatial variations for $\vartheta(\mathbf{x})$. This happens for instance when focusing on the flow below the core of the nuclear reactor, or when investigating the flow in steam generators. A typical situation corresponds to the fluid flow coming from a pure fluid zone and entering a domain obstructed with tiny aligned tubes. This case has been investigated some time ago in [15] for instance. It has been pointed out in this work

that the conditions that are enforced at the steady interface associated with the discontinuity in the porous profile, which correspond to the preservation of Riemann invariants of the steady wave, do not match the true behaviour of the fluid properties, as revealed by the multi-dimensional computations. More precisely, the mass flow rate $\vartheta \underline{Q}.\underline{n}$ and the energy flow rate $\vartheta \underline{Q}.\underline{n}H$ are indeed physical invariants, but the third Riemann invariant is actually not preserved. This in fact is almost obvious, and known from long ; it simply means that some **singular** head losses have been omitted in the basic formulation of the momentum balance, which in turn results in this mismatching.

Thus, a straightforward cure simply consists in recovering these singular head losses. This is precisely what has been achieved in the recent paper [1] within the framework of one-dimensional flows in pipes with varying cross sections. The main objective here is to build the counterpart of this approach in a multidimensional domain occupied by the fluid and many obstacles. As it will quickly occur, the idea is almost trivial.

Hence the paper is organised as follows. In section 2, we first present an integral approach in order to get approximate solutions of a compressible flow model, when the fluid evolves in a large domain obstructed by many small obstacles. The target model will be the Euler set of equations. In section 3, we will briefly detail the counterpart of Bernouilli formulas for compressible flows encountering a sudden contraction. Section 4 will give focus on some approximate/exact solutions of compressible fluids flowing in a free medium and then crossing a contraction. These test cases are highly representative of what may happen in industrial applications for nuclear power plant studies. Then, section 5 will give the main ingredients of the numerical algorithms involved ; those mainly rely on standard approximate Riemann solvers, but of course implicit numerical solvers that aim at coping with low-Mach number flows might be considered as well. We will present afterwards some numerical results in the last section. A comparison of results associated with:

1. the two-dimensional approximate solution obtained on a very fine grid, which will be refered to as the "reference" solution,

2. the integral two-dimensional approach proposed in the present paper,

will be achieved. Moreover, these two-dimensional results will be compared with those provided by the classical one-dimensional well-balanced approach associated with the simulation of solutions of (1) (see appendix B), and also with those pertaining to the one-dimensional integral approach of [1]. When available, the measure of the L^1 norm of the error will be provided. An appendix devoted to viscous effects completes the whole.

2 Basic formulation

2.1 Set of equations

We consider the compressible Navier-Stokes equations. As usual, the main unknowns ρ, $\underline{u}$, P respectively denote the density, the velocity, and the pressure of the fluid. The mean total energy E is such that :

$$E = \rho((\underline{u})^2/2 + \epsilon(P,\rho))$$

and the momentum is: $\underline{Q} = \rho\underline{u}$. The internal energy $\epsilon(P,\rho)$ must be prescribed by the user.

The speed of acoustic waves, which will be noted c, is such that:

$$c^2 = \left(\frac{P}{\rho^2} - \frac{\partial\epsilon(P,\rho)}{\partial\rho}\right)/(\frac{\partial\epsilon(P,\rho)}{\partial P})$$

Thus the set of governing equations is:

$$\begin{cases} \dfrac{\partial\rho}{\partial t} + \nabla.(\underline{Q}) = 0 \\ \dfrac{\partial\underline{Q}}{\partial t} + \nabla.(\underline{Q}\otimes\underline{Q}/\rho) + \nabla P = \nabla.\left(\underline{\underline{\Sigma^v}}\right) \\ \dfrac{\partial E}{\partial t} + \nabla.\left(\underline{Q}(E+P)/\rho\right) = \nabla.\left(\underline{\underline{\Sigma^v}}\,\underline{u}\right) \end{cases} \tag{2}$$

when neglecting Fourier heat flux contributions. We also note :

$$H = (E+P)/\rho$$

the total enthalpy, and $h = \epsilon + P/\rho$ is the specific internal enthalpy. The viscous stress tensor $\underline{\underline{\Sigma^v}}$ is briefly recalled though classical:

$$\underline{\underline{\Sigma^v}} = \mu(\underline{\underline{D}} - \frac{1}{3}trace(\underline{\underline{D}})Id)$$

with:

$$\underline{\underline{D}} = \left(\nabla u + \nabla^T u\right)/2$$

thus assuming a minimum entropy dissipation.

Smooth solutions of (2) comply with the entropy inequality:

$$\frac{\partial\eta}{\partial t} + \nabla.(\underline{F_\eta}) \leq 0$$

where ($\eta = \rho s, \underline{F_\eta} = \rho s\underline{u}$) denotes the entropy-entropy flux pair, and $s(P,\rho)$ complies with:

$$c^2(P,\rho)\frac{\partial s(P,\rho)}{\partial P} + \frac{\partial s(P,\rho)}{\partial\rho} = 0$$

Throughout the paper, W will be the conservative variable:

$$W = (\rho, \underline{Q}, E)^t$$

2.2 Integral form of conservation laws

We will now integrate the set of equations on a control volume Ω_i that may contain many obstacles. These obstacles may be completely included in it, or cross it totally or partially; of course part of the boundary of this control volume may coincide with the surface of an obstacle. A sketch of the different admissible situations is provided in figure 1.

In the following, the upperscript ϕ_{ij} refers to interfaces ij separating two neighbouring control volumes Ω_i and Ω_j where the fluid may cross the ij interface. The corresponding surface is noted S_{ij}^{ϕ}.

On the contrary, upperscripts w_i refer to interfaces where a wall boundary Γ_i^w is present (strictly) inside the control volume Ω_i or on the boundary of the control volume Ω_i. The corresponding surface is noted S_i^w. Obviously, the mass flux is null through the latter surface S_i^w.

Eventually, the volume occupied by the fluid within the control volume Ω_i is denoted Ω_i^{ϕ}.

Nonetheless, a "big" control volume Ω_i may contain several ($k \in 1, N(i)$) fluid sub-domains $\Omega_{i,k}^{\phi}$, that are not connected to each other; this is due to the fact that tiny obstacles may fully split Ω_i into smaller -non connected- control volumes. This happens when elements of type (3) are present within cell i (see figure (1)). Hence we need to introduce within each fluid sub-cell $\Omega_{i,k}^{\phi}$ a mean value of the fluid state variable $W(\mathbf{x}, t)$ noted $W_{i,k}(t)$:

$$W_{i,k}(t) = \left(\int_{\Omega_{i,k}^{\phi}} W(\mathbf{x}, t) dx \right) / meas(\Omega_{i,k}^{\phi})$$

and we also introduce a natural definition for the mean fluid state variable in cell $W_i(t)$ as:

$$W_i(t) = \left(\int_{\Omega_i^{\phi}} W(\mathbf{x}, t) dx \right) / meas(\Omega_i^{\phi})$$

while:

$$\Omega_i^{\phi} = \cup_{k \in 1, N(i)} \Omega_{i,k}^{\phi}$$

Thus:

$$W_i(t) = \left(\sum_{k \in 1, N(i)} meas(\Omega_{i,k}^{\phi}) W_{i,k}(t) \right) / meas(\Omega_i^{\phi})$$

which guarantees a consistent formula for $W_i(t)$, since:

$$meas(\Omega_i^{\phi}) = \sum_{k \in 1, N(i)} meas(\Omega_{i,k}^{\phi})$$

We may now consider the conservation law:

$$\frac{\partial W}{\partial t} + \nabla.(\underline{F}(W)) = \nabla.(\underline{F^v}(W, \nabla W))$$

and integrate over time interval $[t_1, t_2]$ and space with respect to $\Omega_{i,k}^{\phi}$; hence we get:

$$\int_{\Omega_{i,k}^{\phi}} (W(\mathbf{x}, t_2) - W(\mathbf{x}, t_1))dx + \int_{t_1}^{t_2} \int_{\Gamma_{i,k}} \underline{F}(W(\mathbf{x}, t)).\underline{n}d\gamma = \int_{t_1}^{t_2} \int_{\Gamma_{i,k}} \underline{F^v}(W(\mathbf{x}, t), \nabla W(\mathbf{x}, t)).\underline{n}d\gamma$$

with $\underline{F}(W(\mathbf{x}, t)$ the convective flux and $\underline{F^v}(W(\mathbf{x}, t), \nabla W(\mathbf{x}, t))$ the diffusive flux. Here, $\Gamma_{i,k}$ denotes the whole boundary of the fluid sub-cell $\Omega_{i,k}^{\phi}$. We may also distinguish the fluid and the wall boundaries $\Gamma_{i,k}^{\phi}$ and $\Gamma_{i,k}^{w}$ of each sub-cell $\Omega_{i,k}^{\phi}$, such that:

$$\Gamma_{i,k} = \Gamma_{i,k}^{\phi} \cup \Gamma_{i,k}^{w}$$

We also have:

$$\underline{F}(W).\underline{n} = (\rho \underline{u}.\underline{n}, (\rho \underline{u}.\underline{n})\underline{u} + P\underline{n}, (E + P)\underline{u}.\underline{n})$$

Summing up over the $N(i)$ fluid sub-cells, we get at once:

$$\begin{aligned} meas(\Omega_i^{\phi})(W_i(t_2) - W_i(t_1)) + \sum_{k \in 1, N(i)} (\int_{t_1}^{t_2} \int_{\Gamma_{i,k}} \underline{F}(W(\mathbf{x}, t)).\underline{n}d\gamma) \\ = \sum_{k \in 1, N(i)} (\int_{t_1}^{t_2} \int_{\Gamma_{i,k}} \underline{F^v}(W(\mathbf{x}, t), \nabla W(\mathbf{x}, t)).\underline{n}d\gamma) \end{aligned} \tag{3}$$

These formulas are actually an integral approach that will be used afterwards. We insist on the fact that in some particular situations, the counterpart of the control volume, which will be the Finite Volume cell, may contain obstacles of type (3) (see figure 1) such that mean values $W_{i,k}(t)$ are completely different from one another. This may happen for instance in tube bundles in the core of a nuclear reactor, or in steam generators. The first test case in section 6 will refer to this specific situation.

However, **in the sequel**, we will get rid of viscous contributions. Some way to account for these contributions is discussed in appendix A. We recall that one main goal here is to compare various formulations, including the true multi-dimensional approach, the integral approach, and the classical porous approach. Thus a more accurate way to achieve that amounts to consider the sole convective terms. Hence we will now focus on:

$$\begin{aligned} meas(\Omega_i^{\phi})(W_i(t_2) - W_i(t_1)) + \sum_{k \in 1, N(i)} (\int_{t_1}^{t_2} \int_{\Gamma_{i,k}^{\phi}} \underline{F}(W(\mathbf{x}, t)).\underline{n}d\gamma) \\ + \sum_{k \in 1, N(i)} (\int_{t_1}^{t_2} \int_{\Gamma_{i,k}^{w}} \underline{F}(W(\mathbf{x}, t)).\underline{n}d\gamma) = 0 \end{aligned} \tag{4}$$

The integral formulation (4) simply represents - in spirit- the counterpart of the classical Finite Volume approach, using a double integration wrt time and space on some given -steady- control volumes. The main difference here with the usual FV approach is that the formulation is continuous (and not discrete), and also that the boundary of control volumes is no longer assumed to fit perfectly the wall boundaries arising with obstacles, as it happens in the classical "pure CFD" FV approach.

Before going further on, we discuss in the following sections some approximate form of Bernouilli conditions, and also provide some exact and approximate solutions for two test cases.

3 An approximation of singular head losses encountered in sudden contractions

We focus here on the integral form of conservation laws around some **steady** state. The fluid is thus assumed to be flowing in a uniform pipe of section S^- and then entering a second pipe with a different section S^+. We detail constraints associated with the left state $(\rho, U, P)^-$ and the right state $(\rho, U, P)^+$, denoting P^* (respectively P^{**}) the mean pressure acting on the wall boundary of surface $(S^- - S^+)$ when $S^- > S^+$ (respectively $(S^+ - S^-)$ when $S^- < S^+$).

Some straightforward calculations yield in the first case ($S^- > S^+$):

$$\left\{ \begin{array}{l} [\rho U S]_-^+ = 0 \\ [(\rho U^2 + P)S]_-^+ + P^*(S^- - S^+) = 0 \\ [\rho U H S]_-^+ = 0 \end{array} \right. \tag{5}$$

A reasonable estimate for P^* is the wall value of the pressure associated with a symmetric Riemann problem, where the initial left state is $W_L = W^-$, while the initial right state is $W_R = \hat{W_L}$, if $\hat{a}$ denotes the mirror state of a with respect to $\mathbf{n} = \mathbf{n_x}$; thus:

$$P^* = P^{Riemann}(W^-, \hat{W^-}, \mathbf{n} = \mathbf{n_x})$$

Similar computations can be performed in the second case when $S^- < S^+$:

$$\left\{ \begin{array}{l} [\rho U S]_-^+ = 0 \\ [(\rho U^2 + P)S]_-^+ - P^{**}(S^+ - S^-) = 0 \\ [\rho U H S]_-^+ = 0 \end{array} \right. \tag{6}$$

In that second case, the wall pressure P^{**} may be estimated as:

$$P^{**} = P^{Riemann}(\hat{W^+}, W^+, \mathbf{n} = -\mathbf{n_x})$$

In the first case, the mass balance and the momentum balance enable to rewrite:

$$\left\{ \begin{array}{l} (\rho S)^+ [U]_-^+ + U^- [\rho S]_-^+ = 0 \\ \overline{\rho U S}[U]_-^+ + S^+ [P]_-^+ + (P^- - P^*)[S]_-^+ = 0 \end{array} \right. \tag{7}$$

where:

$$\overline{\rho U S} = ((\rho U S)^+ + (\rho U S)^-)/2 = (\rho S)^+ \overline{U} - \frac{U^-}{2}[\rho S]_-^+$$

Then, inserting the latter expression in the second equation of (7), and eliminating $[\rho S]_-^+$ from the first equation in (7), we get:

$$(\rho S)^+ [U^2/2]_-^+ + (\rho S)^+ ([U]_-^+)^2/2 + S^+ [P]_-^+ + (P^- - P^*)[S]_-^+ = 0$$

Now, if we restrict to a perfect gas EOS ($P = (\gamma - 1)\rho\epsilon(P, \rho)$), we can give the explicit form of P^* which is:

$$P^* = P^- \left(1 + f(\frac{U^-}{c^-})\right)$$

with : $f(0) = 0$ and $f'(0) = \gamma$. For small enough values of the local Mach number $|\frac{U^-}{c^-}|$, we get an approximation $P^* = P^-$, thus:

$$[U^2/2]^+_- + \frac{1}{\rho^+}[P]^+_- = -\frac{1}{2}([U]^+_-)^2 < 0 \tag{8}$$

The exact form is in fact:

$$[U^2/2]^+_- + \frac{1}{\rho^+}[P]^+_- = -\frac{1}{2}([U]^+_-)^2 + \frac{P^-}{(\rho S)^+} f(\frac{U^-}{c^-})[S]^+_- \tag{9}$$

The second contribution on the right hand side will be negative (respectively positive) if the fluid at the left inlet is moving towards the right (resp. to the left), since in that case we have: $[S]^+_- < 0$, and: $f(\frac{U^-}{c^-}) > 0$ (resp. $f(\frac{U^-}{c^-}) < 0$).

In the second case, where $[S]^+_- > 0$, we rewrite mass and momentum balance as follows:

$$\begin{cases} (\rho S)^-[U]^+_- + U^+[\rho S]^+_- = 0 \\ \overline{\rho U S}[U]^+_- + S^-[P]^+_- + (P^+ - P^{**})[S]^+_- = 0 \end{cases} \tag{10}$$

Hence, since:

$$\overline{\rho U S} = (\rho S)^- \overline{U} + \frac{U^+}{2}[\rho S]^+_-$$

we eventually get:

$$(\rho S)^-[U^2/2]^+_- - (\rho S)^-([U]^+_-)^2/2 + S^-[P]^+_- + (P^+ - P^{**})[S]^+_- = 0$$

or:

$$[U^2/2]^+_- + \frac{1}{\rho^-}[P]^+_- = \frac{1}{2}([U]^+_-)^2 + \frac{P^+}{(\rho S)^-} g(\frac{U^+}{c^+})[S]^+_- \tag{11}$$

with $g(y) = f(-y)$.

This extension (11) of the Bernouilli relations for discontinuous cross sections is obviously the counterpart of the previous case (9). The singular head losses actually increase when the fluid flows from the larger pipe to the pipe of smaller cross section. We emphasize that these results are valid in the framework of stiffened gas EOS or other more complex EOS. We also recall that specific and detailed formulations of head losses can be found in [24] for instance.

We eventually recall that the classical one-dimensional variable cross-section approach (or alternatively the standard porous approach) relies on the use of the set of governing equations:

$$\begin{cases} \dfrac{\partial \rho S}{\partial t} + \dfrac{\partial \rho S u}{\partial x} = 0 \\ \dfrac{\partial \rho S u}{\partial t} + \dfrac{\partial \rho S u^2}{\partial x} + S\dfrac{\partial P}{\partial x} = 0 \\ \dfrac{\partial E S}{\partial t} + \dfrac{\partial u(E+P)S}{\partial x} = 0 \\ \dfrac{\partial S}{\partial t} = 0 \end{cases} \tag{12}$$

and on the use of Riemann invariants of the steady wave across abrupt changes of section in order to connect states W^- and W^+. Unless the flow is at rest, this results in the following three constraints:

$$\begin{cases} [\rho u S]_-^+ = 0 \\ [u^2/2 + \epsilon(P,\rho) + \frac{P}{\rho}]_-^+ = 0 \\ [\eta(P,\rho)/\rho]_-^+ = 0 \end{cases} \tag{13}$$

or equivalently:

$$\begin{cases} [\rho u S]_-^+ = 0 \\ [u^2/2 + \int^\rho (\frac{c^2(\rho,\eta)}{\rho} d\rho)]_-^+ = 0 \\ [\eta(P,\rho)/\rho]_-^+ = 0 \end{cases} \tag{14}$$

Note that when restricting to perfect gas EOS, we retrieve the classical relation: $[\frac{u^2}{2} + \frac{c^2}{\gamma - 1}]_-^+ = 0$. Though different, these constraints (13) (or (14)) may be compared with (5) (or (6)).

Eventually we underline the fact that numerical approximations of solutions that have been investigated in references [14, 25] rely on exact solutions of the Riemann problem associated with conditions (13). Note also that most of current "true" well-balanced schemes in the literature have been designed using relations (13).

Actually, test B in section 4 will stand for the counterpart of this global balance of mass, momentum and energy that has been examined in section 3. The quantity P^* in equation (15), which represents the integral of pressure forces on vertical wall faces arising with obstacles aligned in the flow direction, will be computed with a two-dimensional CFD code. This will allow the derivation of outlet conditions on the right hand side (by finding $X^\pm$ densities at the right exit, which are solutions of equation (16)) and will give some reference solution.

4 Two basic test cases

4.1 Test A

This first test case is indeed very simple. It simply consists in computing the flow of a fluid along aligned obstacles, in a two-dimensional framework. Obstacles are identical (these may represent tube bundles in a steam generator or in the core of a reactor in a nuclear power plant). A sketch of the test case is displayed on figure (2).

Since viscous effects are neglected, and due to the fact that all flows are separated by obstacles, we may examine the influence of the mesh refinement, and compute the error for all meshes. Within the area contained between two aligned tubes (for $m = 1$ to 3), the steady flow complies with:

$$\rho(x,y,t) = \rho_L^m \quad ; \quad U(x,y,t) = U_L^m \quad ; \quad V(x,y,t) = 0 \quad ; \quad P(x,y,t) = P_L^m$$

where ρ_L^m, U_L^m, P_L^m respectively denote values enforced on the left side corresponding with the inlet boundary. Values will be chosen different within each sub-channel in order to check the mesh dependency. Detailed values of constants (ρ_L^m, U_L^m, P_L^m) will be given in section 6.1.

4.2 Test B

We consider here the flow of a compressible fluid entering a domain including many aligned tubes. The flow is assumed to be steady, and we moreover impose that the mean flow direction at the inlet -on the left side- would be aligned with the symmetry axis of obstacles (see figure (8)).

Symmetry -or equivalently wall- conditions are enforced on the upper and lower part of the computational domain. A straightforward integration of mass, energy and $x-$ momentum equations immediately provides:

$$\begin{cases} \rho_2 U_2 S_2 = \rho_1 U_1 S_1 = Q_1 \\ h(P_2,\rho_2) + U_2^2/2 = h(P_1,\rho_1) + U_1^2/2 = H_1 \\ (\rho_2 U_2^2 + P_2) S_2 - (\rho_1 U_1^2 + P_1) S_1 + P^*(S_1 - S_2) = 0 \end{cases} \tag{15}$$

Values $\rho_1, U_1, P_1, S_1, S_2$ are given and the unknown is (ρ_2, U_2, P_2). We also assume an initial and relevant guess for P^*.

We consider the main unknown $X = \rho_2$, we may achieve some basic calculations and get that X is solution of the scalar equation:

$$g(X) = H_1 \tag{16}$$

where:

$$g(X) = h(\mathcal{P}_1 - (\frac{Q_1}{S_2})^2/X, X) + \frac{1}{2}\left(\frac{Q_1}{X S_2}\right)^2 \tag{17}$$

setting:

$$\mathcal{P}_1 = ((\rho_1 U_1^2 + P_1)S_1/S_2 + P^*(1 - S_1/S_2)) \tag{18}$$

If we assume a perfect gas state law:

$$P = (\gamma - 1)\rho\epsilon$$

then : $h(P, \rho) = \frac{\gamma P}{(\gamma-1)\rho}$, and we may set: $\beta = \frac{\gamma+1}{\gamma-1}$. Hence X must be solution of :

$$H_1 X^2 - \frac{\gamma}{\gamma - 1}\mathcal{P}_1 X + \frac{\beta Q_1^2}{2S_2^2} = 0$$

When solutions X^+, X^- are real, both are positive since $H_1 > 0$ and $\mathcal{P}_1 > 0$. Eventually, we get the velocity U_2

$$U_2 = Q_1/(S_2 X)$$

and:

$$P_2 = \mathcal{P}_1 - (\frac{Q_1}{S_2})^2/X$$

These solutions will be used in section 6.2. Note that the value P^* will be computed using numerical approximations of the solution in the multi-D case on a very fine mesh.

Once more, we emphasize that this solution may be used whatever the EOS is, using relations (16), (17), (18) ; of course expressions that have been detailed afterwards should be modified consequently.

5 Numerical schemes

The numerical algorithm that has been used to get approximations of solutions of system (4) is described below. It is assumed that all numerical fluxes may be evaluated by means of standard Finite volume techniques, considering one mean value W_i^n per cell Ω_i at each time t^n. This is obviously questionable, especially when some tiny obstacles split the cell Ω_i into several subcells which are not connected (element 3 in figure (1)). By the way this is one of the reasons that motivated the investigation of test case A. Actually, in this particular case where sub-channels are fully decoupled, the mean value over a control volume overlapping a tube may lead to unrealistic values of the mean state variable. This will be discussed in section 6.1.

Hence we assume that W_i^n is an approximation of $W_i(t^n)$, and denote as usual the time step: $\Delta t^n = t^{n+1} - t^n$. Moreover, we focus in this paper on **explicit** formulations. We define the following scheme:

$$\begin{aligned} meas(\Omega_i^\phi)(W_i^{n+1} - W_i^n) + \Delta t^n \sum_{k=1,N(i)} \left(\sum_{(j,k')\in V(i,k)} \left(\underline{\mathcal{F}}_n^h\right)_{\Gamma_{i,k/j,k'}^\phi} S_{\Gamma_{i,k/j,k'}^\phi} \right) \\ + \Delta t^n \sum_{k=1,N(i)} \left(\sum_{\Gamma_{i,k}^w} \left(0, (\int_{\Gamma_{i,k}^w} P\underline{n} d\gamma)^h, 0 \right)^t \right) = 0 \end{aligned} \tag{19}$$

since $(\underline{u}.\underline{n}) = 0$ on the wall boundaries. $V(i,k)$ refers to sub-cells $\Omega_{j,k'}^\phi$ that are connected to sub-cell $\Omega_{i,k}^\phi$ through a fluid-fluid interface $\Gamma_{i,k/j,k'}^\phi$. It thus remains to define fluid-fluid and wall boundary numerical fluxes $\underline{\mathcal{F}}_n^h$ and $(\int_{\Gamma_{i,k}^w} P\underline{n} d\gamma)^h$ respectively.

1. Numerical fluxes at fluid-fluid interfaces are chosen in the classical literature. In practice here, all simulations considered in this paper rely on the approximate Godunov scheme VFRoe-ncv using symetrizing variables $Z^t = (s, \underline{u}, P)$, that was introduced in [13]. Hence, setting:

$$\underline{\mathcal{F}_n}(W, \underline{n}) = \left((\underline{Q}.\underline{n}), (\underline{Q}.\underline{n})\underline{u} + P\underline{n}, (\underline{Q}.\underline{n})H \right)^t$$

$\underline{\mathcal{F}}_n^h$ will simply refer to:

$$\underline{\mathcal{F}}_n^h = \underline{\mathcal{F}_n}\left(W_{i,k/j,k'}^*, \underline{n}_{i,k/j,k'} \right) \tag{20}$$

where the unit normal $\underline{n}_{i,k/j,k'}$ points out from sub-cell $\Omega_{i,k}^\phi$ towards sub-cell $\Omega_{j,k'}^\phi$, and where the interface state $W_{i,k/j,k'}^*$ is computed by solving exactly the linear Riemann problem associated with:

$$\begin{cases} \dfrac{\partial s}{\partial t} + \hat{u}_n \dfrac{\partial s}{\partial n} = 0 \\ \dfrac{\partial u_n}{\partial t} + \hat{u}_n \dfrac{\partial u_n}{\partial n} + \frac{1}{\hat{\rho}} \dfrac{\partial P}{\partial n} = 0 \\ \dfrac{\partial P}{\partial t} + \hat{u}_n \dfrac{\partial P}{\partial n} + \rho \hat{c^2} \dfrac{\partial u_n}{\partial n} = 0 \\ \dfrac{\partial u_\tau}{\partial t} + \hat{u}_n \dfrac{\partial u_\tau}{\partial n} = 0 \end{cases} \tag{21}$$

where $u_n = \underline{u}.\underline{n}$, $\underline{n}.\underline{\tau} = 0$, $\underline{\tau}.\underline{\tau} = 1$ and : $u_\tau = \underline{u}.\underline{\tau}$, and also defining an average $\hat{\psi}$ for any variable ψ as:

$$\hat{\psi} = (\psi_L + \psi_R)/2$$

if subscripts L, R refer to the left and right mean values of the state variable ψ apart from interface L/R.

System (21) represents the two-dimensional system of Euler equations, rewritten in non conservative variables, assuming smooth enough solutions ; using invariance under rotation, one may rewrite equations in the local frame $(\underline{n}, \underline{\tau})$ instead of $(\underline{i}, \underline{j})$, and then neglect transverse derivatives (hence along the $\underline{\tau}$-direction). It is used in order to predict intermediate states in the linearized Riemann problem (in the n-direction), and thus it should not be confused with the non viscous part of system (2), which has the correct conservative form, and thus allows the computation of physically relevant shock solutions. We emphasize that this conservative form (2) is the one that is used for the integral formulation (4).

The exact solution of the 1D Riemann problem associated with (21) and initial conditions Z_L, Z_R on the cell interface L/R is noted $Z^*_{i,k/j,k'}$, and thus we get:

$$W^*_{i,k/j,k'} = W(Z^*_{i,k/j,k'})$$

This completes the definition of fluid-fluid numerical fluxes.

2. We turn now to the wall boundary fluxes. We assume discrete fluxes:

$$\left(\mathcal{P}^h \underline{n}\right)^w_{i,k} S_{\Gamma^w_{i,k}} = P(W_{i,k}) \underline{n}^w_{i,k} S_{\Gamma^w_{i,k}} \tag{22}$$

to be consistent approximations of $\int_{\Gamma^w_{i,k}} P\underline{n} d\gamma$.

Obviously, this implies that all impinging effects or suction effects are neglected within the fluid sub-cell $\Omega^\phi_{i,k}$. Moreover, a straightforward consequence of this approximation is that contributions on inner elements of type (4) as defined

in figure (1) are null, since:

$$\left(\int_{\Gamma_{i,k}^{w,4}} P\underline{n}d\gamma\right)^h = P(W_{i,k})\int_{\Gamma_{i,k}^{w,4}} \underline{n}d\gamma = \underline{0}$$

More sophisticated approximations might be considered, for instance those grounded on the exact solution of the 1D Riemann problem on wall boundaries.

The scheme (19) is now fully defined, considering (20) and (22). Actually, many cells in the computational domain will contain a sole fluid sub-cell; in that case the scheme (19) is equivalent to:

$$meas(\Omega_i^\phi)(W_i^{n+1}-W_i^n)+\Delta t^n \sum_{(j,k')\in V(i)} \left(\underline{\mathcal{F}}_n^h\right)_{\Gamma_{i/j,k'}^\phi} S_{\Gamma_{i/j,k'}^\phi}+\Delta t^n \sum_{\Gamma_i^w} \left(0,\mathcal{P}^h\underline{n},0\right)_i^t S_{\Gamma_i^w} = 0$$

which identifies with the classical Finite Volume formulation for full fluid cells, where:

$$\Omega_i^\phi = \Omega_i$$

In the following, the time step Δt^n will be chosen in agreement with the classical CFL condition arising with the fluid-fluid interface fluxes. We also emphasize that inlet and outlet boundary conditions are classical (see [8]) since these boundaries are fluid-fluid interfaces. We now focus on some numerical results associated with the two test cases introduced in section 3.

6 Numerical results

In this section, we will provide numerical results obtained with four different approaches and schemes. These four schemes are:

- the "2D+" scheme which refers to the integral approach detailed in this paper and applied on non adapted meshes;
- the "2D" scheme corresponding to the pure fluid approach, thus using adapted meshes that do not overlap or intersect obstacles;
- the "WBR" scheme which corresponds to the classical one-dimensional well-balanced approach on variable cross-section ducts using the Kröner-Thanh scheme [26] to approximate interface fluxes;
- the "1D+" scheme refering to the almost one-dimensional approach with one row of coarse two-dimensional cells for the simulation of flows in ducts with variable cross-sections (see [1] for details).

Moreover, for the second test case (test B), a comparison with the analytical solution of the density $X^{\pm}$ detailed in section 4.2 will be added, using a normalization $\phi^{\pm}/\phi_L$, where ϕ either denotes the density, the velocity, the pressure or the entropy.

6.1 Test case A

The two-dimensional computational domain is $\Omega = [0,5] \times [0,1]$. We consider regular and rectangular meshes, with faces aligned with the obstacles. The ratio of the fluid section in the x-direction over the total cross section is equal to 0.6.

Densities, x-velocities and pressures at the inlet sections of the upper, middle and lower channels are respectively ($x_L = 0.$):

$$\rho_{up}(x_L,y,t) = 3. \quad ; \quad U_{up}(x_L,y,t) = 300. \quad ; \quad P_{up}(x_L,y,t) = 3.10^4,$$

$$\rho_{mid}(x_L,y,t) = 2. \quad ; \quad U_{mid}(x_L,y,t) = 200. \quad ; \quad P_{mid}(x_L,y,t) = 2.10^4,$$

$$\rho_{low}(x_L,y,t) = 5. \quad ; \quad U_{low}(x_L,y,t) = 500. \quad ; \quad P_{low}(x_L,y,t) = 5.10^4,$$

A perfect gas state law is used:

$$p = (\gamma - 1)\rho\epsilon$$

with $\gamma = 7/5$. We enforce these inlet boundary conditions and compute a steady state. Thus the true solution is simply a constant solution within each channel, which corresponds with the inlet solution. We only consider four distinct meshes in this paper and refer to [28] for further details and other mesh configurations. The initial values are chosen uniform and equal to:

$$\rho(.,t=0) = 1., \quad U(.,t=0) = 0., \quad V(.,t=0) = 0., \quad P(.,t=0) = 10^4$$

Wall boundary conditions are imposed at the top ($y = 1.$) and at the bottom ($y = 0.$) of the computational domain. The outlet fluxes at the right boundary interfaces ($x = 5.$) are calculated with the VFRoe-ncv scheme considering that the external state is equal to the internal state (which is equivalent to some full upwind approximation).

The first mesh is really coarse since it contains only 2 cells in the y-direction and 15 cells in the mean flow direction. The main "advantage" is that tubes are totally contained within the cells, which means that elements of type (3) (in the sense introduced in figure 1) are present here. The porosity ϑ is uniform and equal to 0.6 (as it will happen with the second mesh below). Thus fluxes on the left vertical inlet involve two distinct contributions : W_{up} and W_{mid} for the upper cell, and W_{mid} and W_{low} for the lower cell. When focusing on the steady state arising with this particular mesh, it occurs that transverse fluxes in the y-direction modify the structure of the expected steady solution. This was expected and is due to the connection of cells in the y-direction through fluid/fluid interfaces that involve mean cell values that are averages of states W_{up}, W_{mid} and W_{low}, which does not make sense at all. It obviously implies that coarse meshes should not overlap regions which are physically non-connected. Then, for each variable $\varphi = (\rho, U, V, P)$, the L^1 norm of the error is defined by :

$$e_{L^1}(\varphi; t^n) = \frac{\sum_{i\in\{1,N_{cells}\}} \left|\varphi_i^n - \varphi_i^{analytical}\right| vol(\Omega_i)}{\sum_{i\in\{1,N_{cells}\}} \left|\varphi_i^{analytical}\right| vol(\Omega_i)}$$

The L^1 norm of the error is of order unity with mesh 1, whatever the variable is.

The second mesh contains only three cells in the transverse y-direction, and 15 cells in the x-direction. This means that the two obstacles no longer split any cell into two fluid subcells that are not connected. The ratio ϑ is still equal to 0.6 everywhere in the computational domain. Steady results are displayed in figure 3, 4, 5, 6, and include the porosity, the Mach number, the x-velocity component, the density and the pressure. The error distribution is also provided for density, pressure and velocity components. It is obviously close to 10^{-12}, or even smaller, almost everywhere.

The third mesh is made of 5×15 cells. Two points that should be noted here are that: (i) some cells are pure solid cells ($\vartheta = 0$) ; (ii) the second row of cells in the y-direction does not perfectly fit the lower wall boundary of the lower tube, since an error has been added on purpose, in order to check the robustness of the code. Thus this mesh is interesting, since it contains pure fluid cells ($\vartheta = 1$), pure solid cells ($\vartheta = 0$), and a second row of cells with very weak porosities ($\vartheta = 10^{-5}/3$). Eventually, a three finer meshes with 6×30, 12×60 and 14×60 regular cells enable to check that the error computed by the code is still close to round-off errors. All results can be found in [28].

The L^1 norm of the error around the steady state has been plotted on figure 7 for all meshes, except for the first one (see the discussion above). We can notice that

the norm of the error is close to round-off errors, which explains the small increase of the L^1 norm when comparing the second (3×15) and the third mesh (5×15).

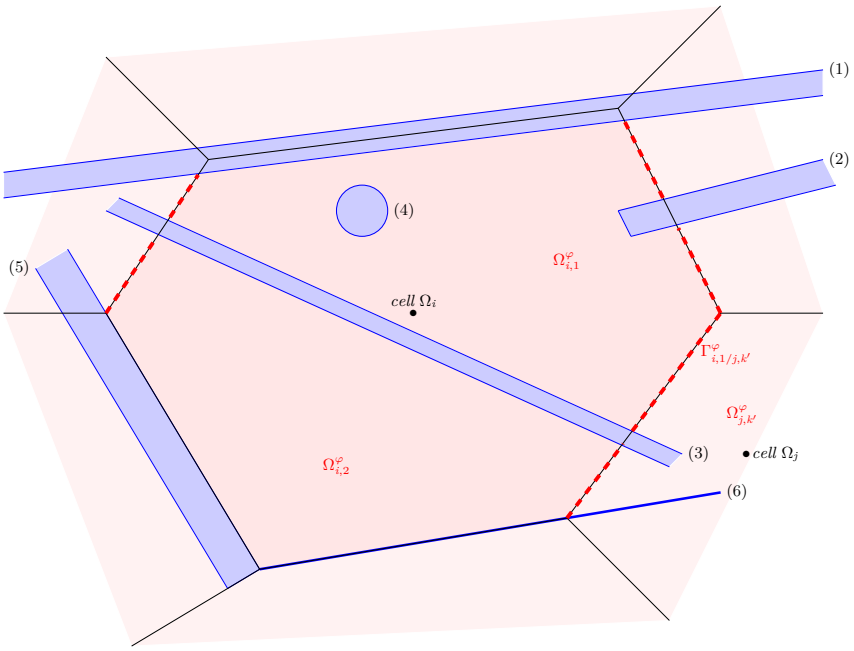

Figure 1: A (pink) control volume Ω_i includes (blue) obstacles numbered from 1 to 5. Obstacles may: be aligned with part of the boundary of cell i (element 5); partially occupy one fluid cell (or subcell) (element 2); fully cross cell i and split it into two fluid sub-cells $\Omega^{\phi}_{i,1}$ and $\Omega^{\phi}_{i,2}$ (element 3); be totally included in cell i or one of its subcells (element 4); overlap part of the boundary of cell i (element 1). The dashed red surface corresponds to the fluid-fluid part of the boundary $\Gamma^{\phi}_{i,k}$ between sub-cells $\Omega_{i,k}$ and their neighbouring sub-cells occupied by the fluid.

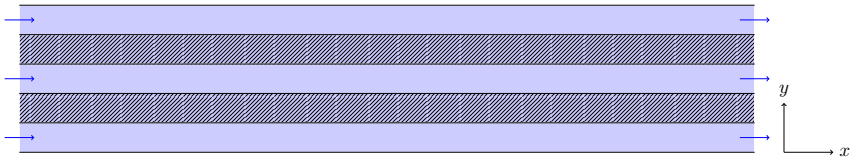

Figure 2: Sketch of test case A. The fluid flows from the three left inlets towards the right. Two identical tubes separate the three sub-channels. Inlet values of the density, velocity and pressure within each sub-channel are given in section 6.1.

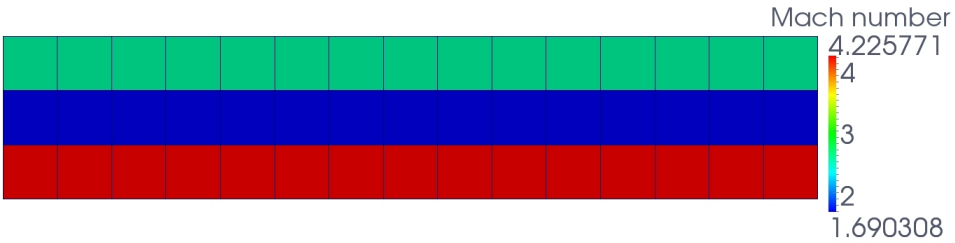

Figure 3: Test case A. Mach number distribution for mesh 2 including 15×3 cells.

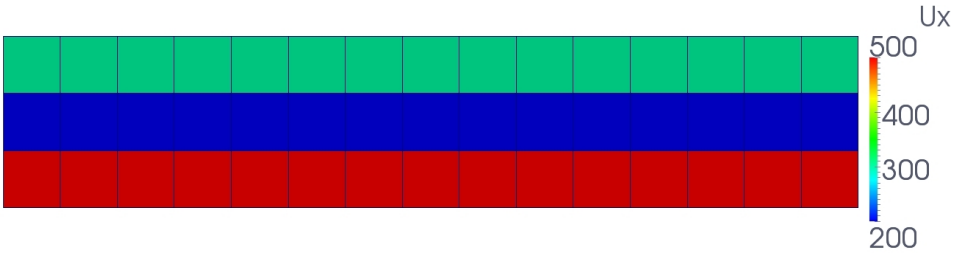

Figure 4: Test case A. Axial velocity distribution for mesh 2 including 15×3 cells.

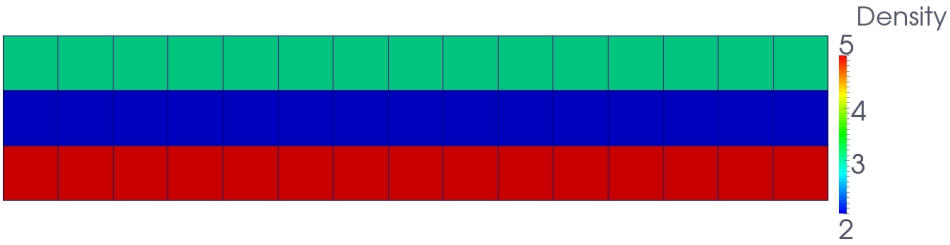

Figure 5: Test case A. Density distribution for mesh 2 including 15×3 cells.

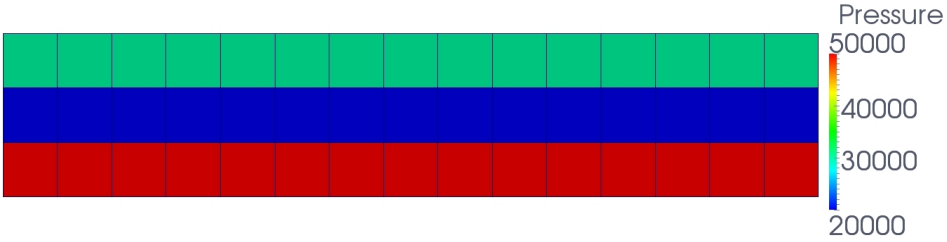

Figure 6: Test case A. Pressure distribution for mesh 2 including 15×3 cells.

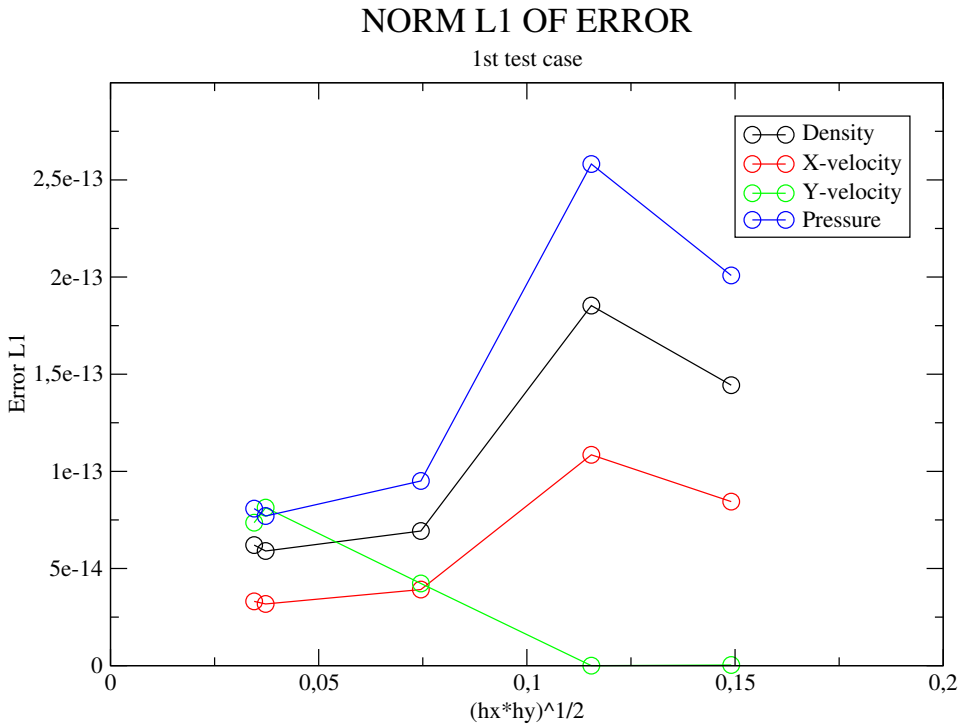

Figure 7: Test case A. L^1 norm of the error versus mesh size h, for the density, velocity and pressure variables. The meshes, from the coarsest (on the right) to the finest (on the left), contain 15×3, 15×5, 30×6, 60×12, and 60×14 cells.

6.2 Test case B

The experiment is somewhat different now, and close to what may happen in practice in some key regions in the coolant circuit in a pressurized water reactor. The inflow of the fluid from the left encounters some region uniformely occupied by two smooth rectangular and aligned tubes. This situation must also be compared with the analytic solution introduced in section 4. Thus the main goal here is to compare:

- the reference solution obtained on the whole computational domain with a reference code solving the Euler equations on a very fine mesh where all wall boundaries are meshed;
- solutions obtained with the integral approach, considering various mesh refinements.

These approximations will also be compared with the exact solution provided in section 4, (using the $P*$ values obtained from the reference solution), and with the one-dimensional integral approach $1D+$ introduced in [1].

The two-dimensional computational domain is now $\Omega = [-15, 5] \times [0, 1]$. The region containing the tubes starts at $x = 2.5$. Computational results will be displayed in the region $[0, 5] \times [0, 1]$. Once again, we use regular rectangular meshes; this enables to fit exactly the wall tube boundaries if necessary. The initial values are chosen uniform and equal to:

$$\rho(., t = 0) = 1., \quad U(., t = 0) = 0., \quad V(., t = 0) = 0., \quad P(., t = 0) = 10^4$$

Symmetry conditions are enforced at the lower and upper parts of the computational domain (respectively for $y = 0.$ and $y = 1.$). Once again, the outlet fluxes at the right boundary interfaces ($x = 5.$) are calculated with the VFRoe-ncv scheme considering the external state equal to the internal state (thus with a full upwind - or "supersonic" - treatment). The left boundary conditions are:

$$\rho(x_L, y, t) = 5. \quad ; \quad U(x_L, y, t) = 500. \quad ; \quad V(x_L, y, t) = 0. \quad ; \quad P(x_L, y, t) = 5.\times 10^4$$

with $x_L = -15$. Computational results are described around the steady state.

The first mesh includes 15×3 cells in the region $[0, 5] \times [0, 1]$. Around the steady state, we plot the cell porosity, Mach number, the $x-$velocity, the density and the pressure on figures 9, 10, 11, 12, 13. We note that the porosity profile is uniform on this coarse mesh in the $y-$direction. As a consequence, the flow seems to behave as a pure one-dimensional flow, thus $y-$components of the velocity are close to zero up to round-off errors. The local time residuals which measure the effective steadiness of the flow are smaller than 3.10^{-4} and 3.10^{-3} for the $x-$velocity and the pressure respectively. Then we turn to the second mesh that involves 16×5 cells in the same domain ; in that case, the mesh perfectly fits the physical wall boundaries, and the porosity is either 1 or null (see figure 14). Similar results for the Mach number and variables U_x, ρ, P are displayed in figures 15, 16, 17, 18. Local time residuals are

higher in that case, due to the occurence of transverse velocities (see figure 19).

The following mesh (mesh 3) is intended to check the stability of the integral approach with respect to the wall boundary fitting. Thus mesh 3 is almost identical to mesh 2, except for the fact that the first -lower- row of cells in the $x-$direction has been slightly moved and their top interfaces are now located at $y = 0.2 + 10^{-5}$ (instead of $y = 0.2$ for the previous mesh). We note that the $y-$velocity profile is still close to a pure symmetric case (see figure 20); besides, the mean presure profile (see figure 21) is indeed close to the previous one.

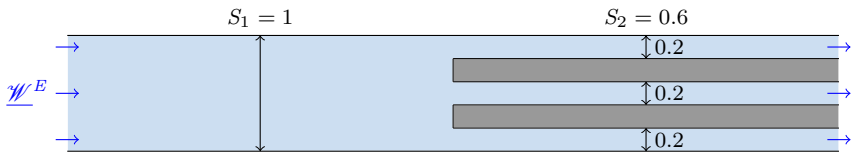

Figure 8: Sketch of test case B. The fluid flows from the left inlet towards the right outlet. On the right hand side, two identical tubes are aligned in the x-direction. The ratio of the right/left flow sections is: $S_R/S_L = 3/5$. Inlet values of the density, velocity and pressure are given in section 6.2.

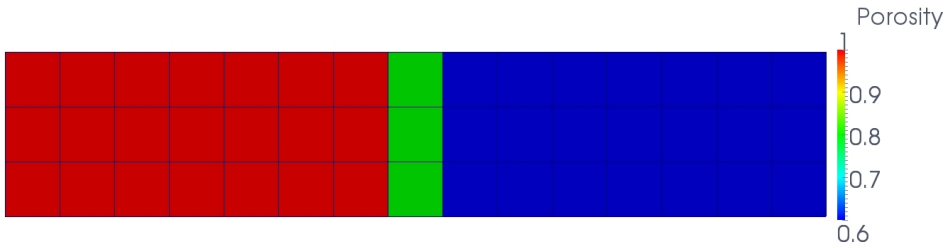

Figure 9: Test case B. Porosity distribution for mesh 1 in region $[0, 5] \times [0, 1]$.

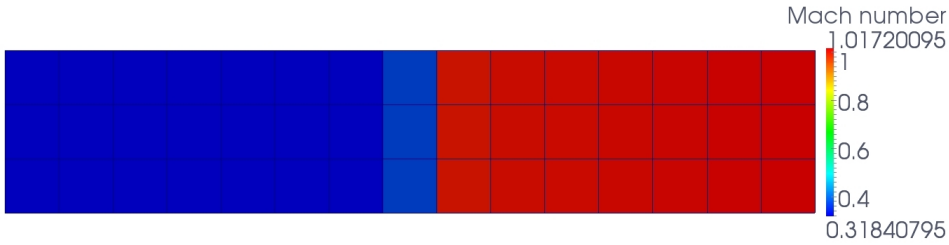

Figure 10: Test case B. Mach number distribution around the steady state for mesh 1 in region $[0, 5] \times [0, 1]$.

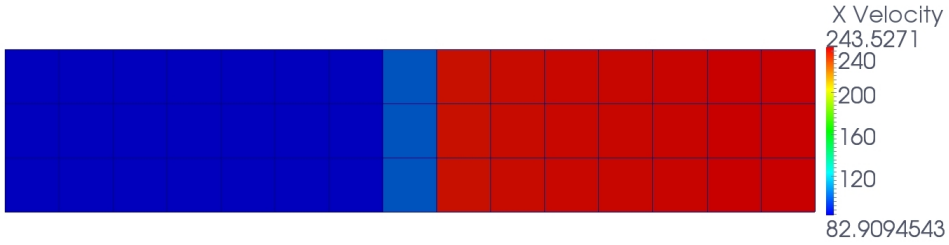

Figure 11: Test case B. Axial velocity distribution around the steady state for mesh 1 in region $[0, 5] \times [0, 1]$.

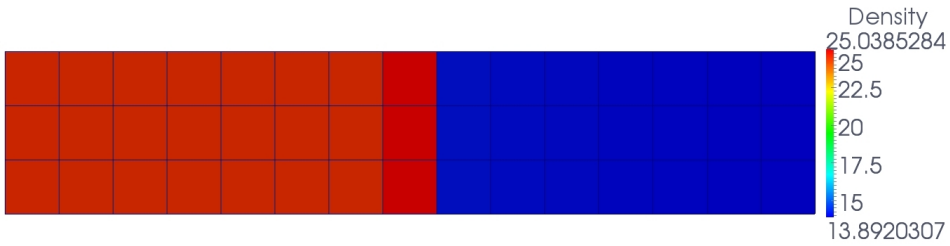

Figure 12: Test case B. Density distribution around the steady state for mesh 1 in region $[0, 5] \times [0, 1]$.

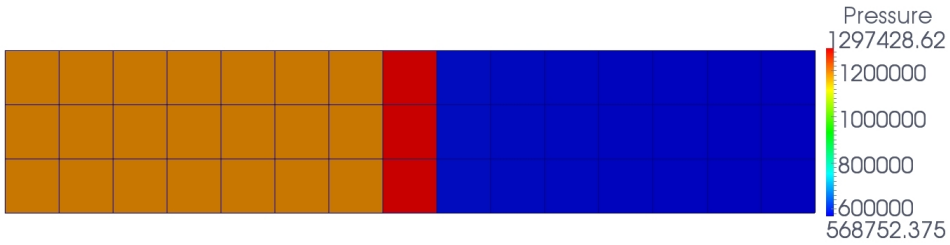

Figure 13: Test case B. Pressure distribution around the steady state for mesh 1 in region $[0, 5] \times [0, 1]$.

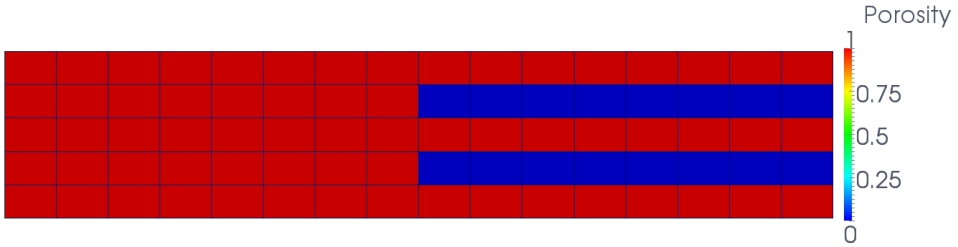

Figure 14: Test case B. Porosity distribution for mesh 2 in region $[0, 5] \times [0, 1]$.

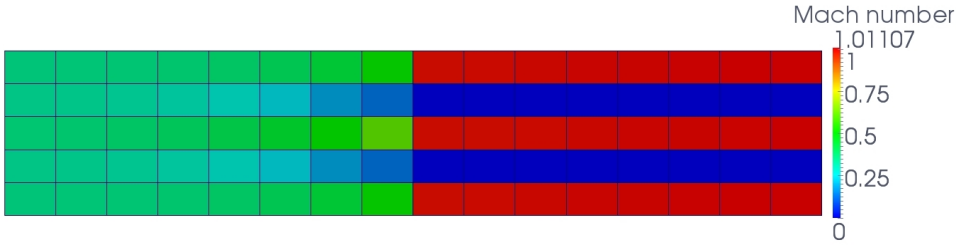

Figure 15: Test case B. Mach number distribution around the steady state for mesh 2 in region $[0, 5] \times [0, 1]$.

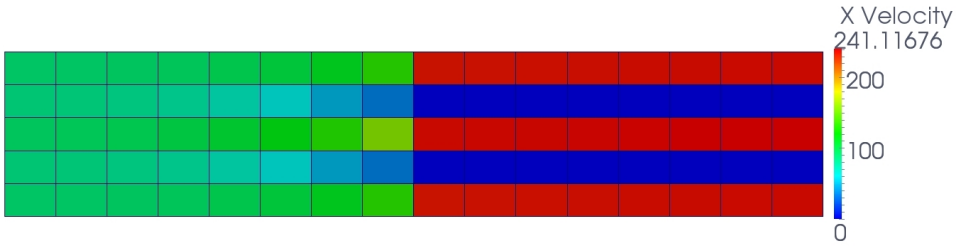

Figure 16: Test case B. Axial velocity distribution around the steady state for mesh 2 in region $[0, 5] \times [0, 1]$.

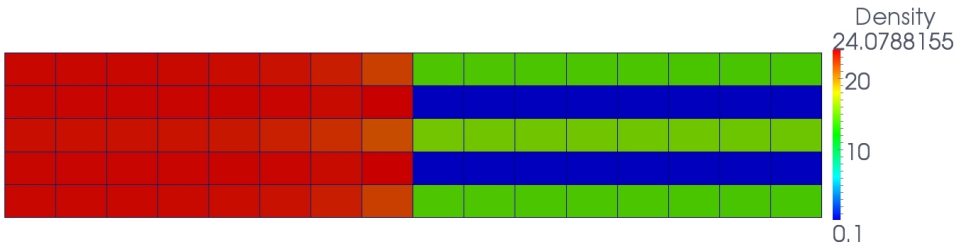

Figure 17: Test case B. Density distribution around the steady state for mesh 2 in region $[0, 5] \times [0, 1]$.

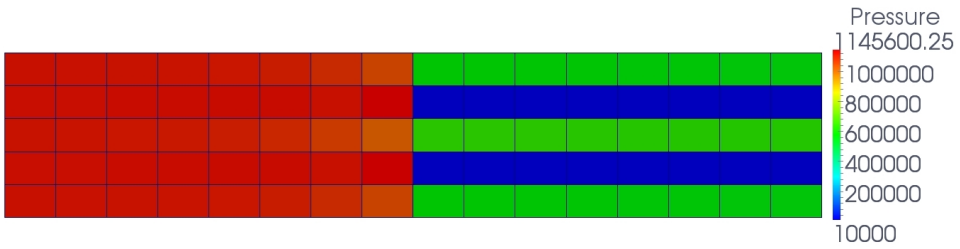

Figure 18: Test case B. Pressure distribution around the steady state for mesh 2 in region $[0, 5] \times [0, 1]$.

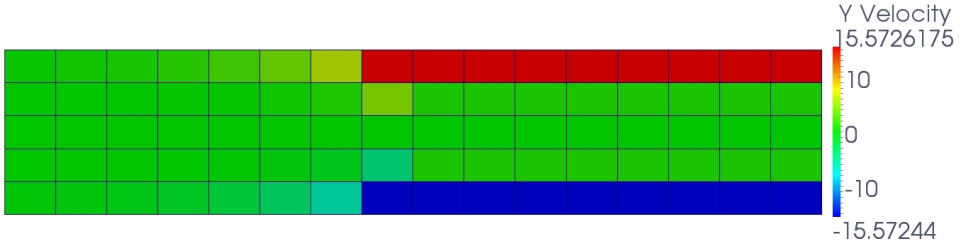

Figure 19: Test case B. Transverse velocity distribution around the steady state for mesh 2 in region $[0, 5] \times [0, 1]$.

The last two meshes are rather fine and contain 375×126 cells and 640×200 cells respectively, still restricting to the region of interest $[0,5] \times [0,1]$. The latter mesh again perfectly fits the wall boundaries, thus the porosity is either 1 or zero, whereas there are some "boundary layers" close the wall boundaries of tubes (where $\vartheta(\mathbf{x})$ lies in $]0,1[$) when focusing on the fourth mesh with 126 cells in the $y-$direction. Density profiles may be compared for the two steady computations (see figures 22 and 23), together with pressure profiles (see figures 24 and 25), and transverse velocity profiles (see figures 26 and 27). The local time residual for the pressure variable is less than 8.10^{-4} for mesh 4 and less than 1.10^{-4} for mesh 5.

Eventually, we may compare results obtained with:

- (i) the "2D+" integral approach (as a function of the mesh size),
- (ii) the analytic solution of section 4.2 that relies on the computation of the densities $X^{\pm}$ solutions of equations (16), (17) and (18);
- (iii) results of the $1D+$ integral approach of [1] (with respect to the mesh size),

with those corresponding to the reference solution ($2D$ approach with only pure fluid cells and wall boundaries).

The reader is refered to figures 28, 29, 30, 31 for that purpose, when focusing on the density, the velocity, the pressure and the entropy respectively.

Obviously, the predicted approximations provided by the well-balanced classical approach (WBR, with $\vartheta = 3/5$), which is based on classical interface conditions, is rather poor, when compared with the $2D+$ approach. This is true for all variables including of course the entropy (see the last figure 31). The $1D+$ scheme performs much better than the WBR approach, as already mentionned in [1], but it remains rather far from results of the $2D+$ approach. This was actually expected here, since the fluid flow indeed contains two-dimensional patterns. Eventually, it may be checked that the $2D$ and $2D+$ appoaches almost coincide when the mesh is refined.

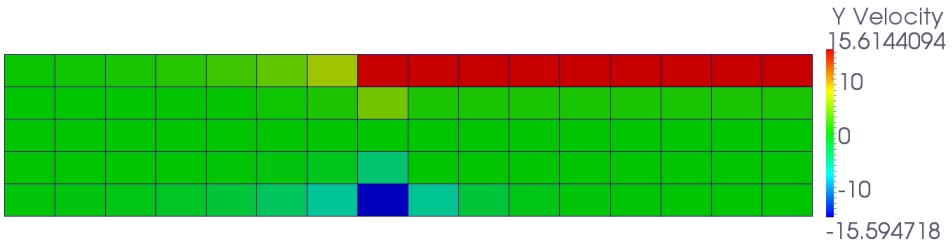

Figure 20: Test case B. Transverse velocity distribution around the steady state for mesh 3 in region $[0, 5] \times [0, 1]$.

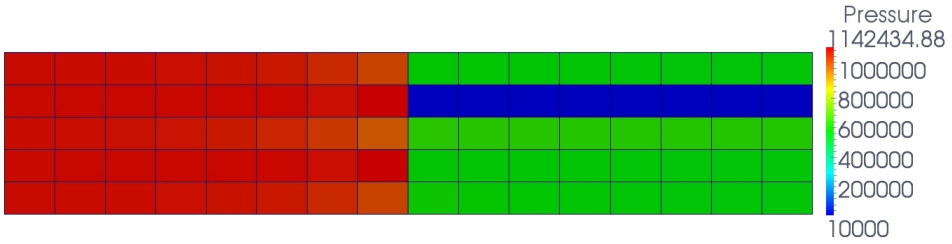

Figure 21: Test case B. Pressure distribution around the steady state for mesh 3 in region $[0, 5] \times [0, 1]$.

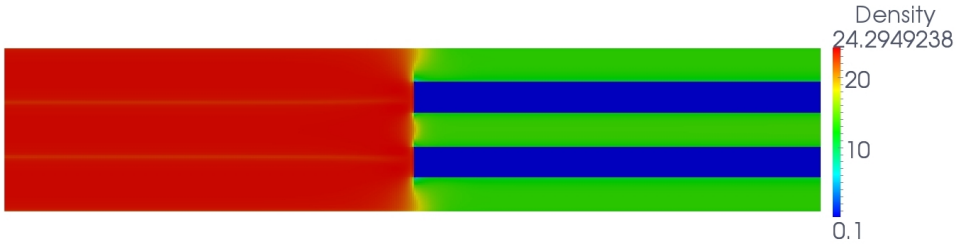

Figure 22: Test case B. Density distribution around the steady state for mesh 4 in region $[0, 5] \times [0, 1]$.

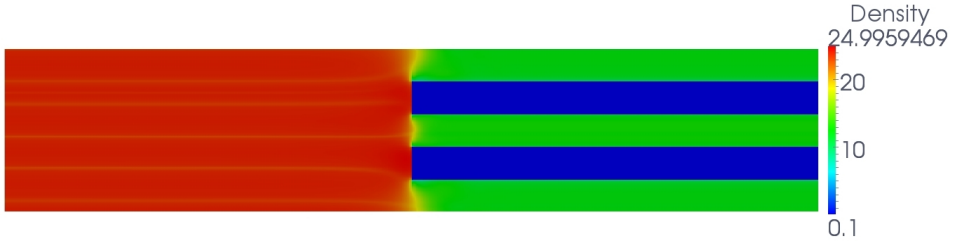

Figure 23: Test case B. Density distribution around the steady state for mesh 5 in region $[0, 5] \times [0, 1]$.

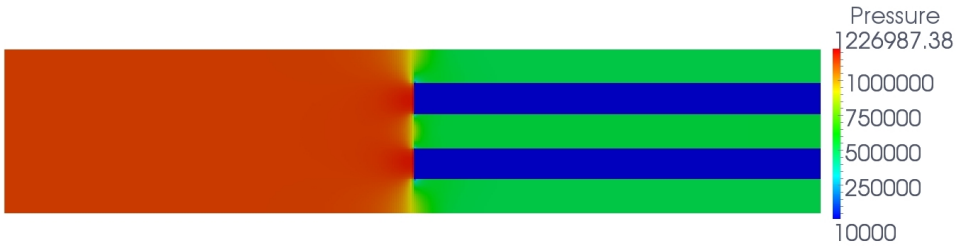

Figure 24: Test case B. Pressure distribution around the steady state for mesh 4 in region $[0, 5] \times [0, 1]$.

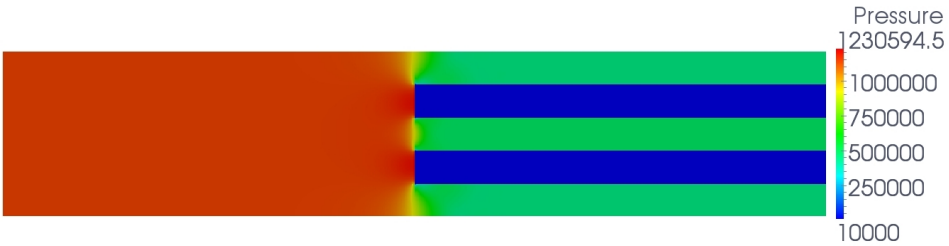

Figure 25: Test case B. Pressure distribution around the steady state for mesh 5 in region $[0, 5] \times [0, 1]$.

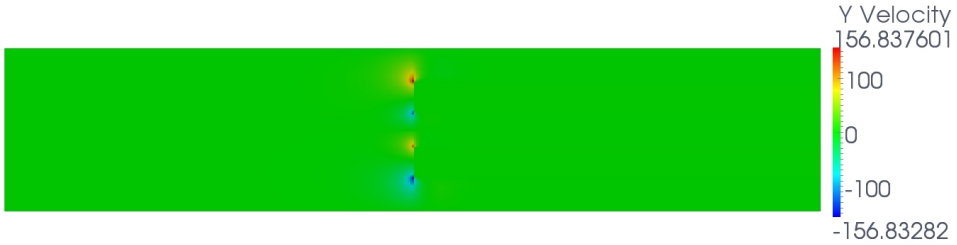

Figure 26: Test case B. Pressure distribution around the steady state for mesh 4 in region $[0, 5] \times [0, 1]$.

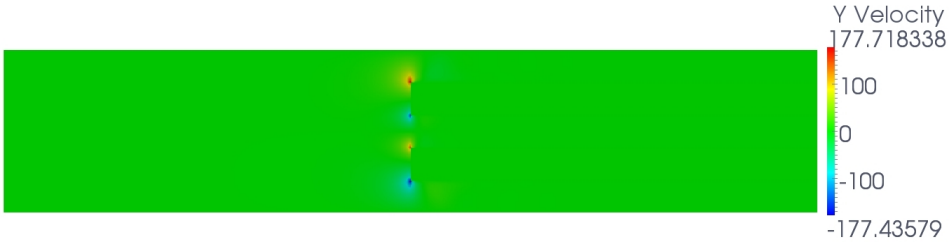

Figure 27: Test case B. Pressure distribution around the steady state for mesh 5 in region $[0, 5] \times [0, 1]$.

7 Conclusion

We presented in this paper an integral approach in order to predict flow patterns of a fluid flowing in a physical domain obstructed by many small obstacles. The basic methodology has been given and discussed, and the main motivations for that work have also been recalled. Numerical results seem to confirm that the basic ideas intially introduced in [1] in a one-dimensional framework are indeed useful and relevant. Numerical simulations obtained with the integral approach have been compared with the "reference" solution that arises when computing the fluid model in the entire fluid domain, while taking all obstacles into account through wall boundary conditions. Results of this comparison are actually quite satisfactory, even when the mesh size is rather coarse, which is of prime interest for nowadays practical computations for nuclear applications. The second essential point to be emphasized is that, by construction, approximate solutions provided by the integral approach naturally converge towards those of the "reference" solution, which is mandatory for nuclear safety reasons. Of course, one cannot afford fine enough meshes for true applications with current computers, and this renders the integral approach really appealing.

Numerical simulations have been run with the help of approximate Riemann solvers at fluid/fluid interfaces. Obviously, the counterpart is straightforward when applying implicit solvers for low-Mach number applications; this further work will be detailed in [28]. Of course, other conservative models may be used in the present integral approach, for instance three or four-equation two-phase flow models. A similar approach may also be used for some non-conservative two-fluid models, such as the one introduced in [21].

Eventually, we also underline that an attempt to use the new connections at steady interfaces, in order to improve the current well-balanced approach, is investigated in a companion work ([22]).

Acknowledgements
Xavier Martin benefits from financial support through an EDF-CIFRE contract 2012/0838. This work has been achieved within the framework of the TITANS2 project. All computational facilities were provided by EDF. Authors thank Bruno Audebert, Martin Ferrand and Erwan Lecoupanec for their help with *Code_Saturne* (see [5]) and for many fruitful discussions. Olivier Hurisse is also acknowledged for his careful reading of the manuscript.

8 Appendix A

This appendix briefly discusses some possible algorithms for the discretization of viscous stress tensors in the integral formulation. Actually, the scheme should provide some approximation of :

$$\int_{\Gamma_{i,k}} \underline{\underline{F^v}}(W(\mathbf{x},t), \nabla W(\mathbf{x},t)) \quad \underline{n} d\gamma$$

on a given control volume Ω_i including obstacles, parts of obstacles, fluid/fluid boundaries and wall boundaries.

The underlying idea simply consists in using standard schemes that enable to account for viscous effects. We refer for that purpose to the basic references [9, 11, 23, 12, 10] and to references therein. We emphasize that the review papers [23, 12] include numerous investigations of approximate solutions of:

$$-\nabla \left(\underline{\underline{K}} \nabla \phi \right) = f$$

(with given Neumann or Dirichlet boundary conditions) when focusing either of Finite Volume schemes, Finite Element schemes, Discontinuous Galerkin schemes, Discrete Duality FV schemes and some others (nonlinear schemes, LB schemes, ...). The tensor $\underline{\underline{K}}$ is assumed to be positive symmetric definite; it may be anisotropic and inhomogeneous, depending on the test cases. Sources terms f arise in some test cases. The two reviews include a thorough comparison of the computational efficiencies, and a measurement of L^2 and L^∞ errors for more than ten distinct cases in a $2D$ or a $3D$ framework, with different -possibly non-conforming- types of meshes. For more details on specific schemes, the reader may also consider companion papers in the above mentionned FVCA5 and FVCA6 proceedings.

1. For wall boundaries, we assume attachment so that :

   $$\underline{u}_{\Gamma^w_{i,k}} = \underline{0}$$

   Hence some rough way to account for viscous effects consists in using a two-point flux approximation, considering a given state $\underline{u}_i^n$ in cell Ω_i at time t^n.

2. If we turn to fluid/fluid interfaces $\Gamma^\phi_{i,k/j,k'}$ separating sub-cells $\Omega^\phi_{i,k}$ and $\Omega^\phi_{j,k'}$, we apply the same strategy, and use a two-point flux approximation for cartesian grids, or SUSHI type schemes for non cartesian grids. We refer to [11] for details.

Of course, implicit schemes should be used in order to get rid of unaffordable time step constraints.

It should be noted that the present strategy enables to handle huge mesh refinements, and thus to converge to the solution of "non-homogeneized" basic solutions of the Navier-Stokes equations when the mesh parameters h and Δt tend to zero.

9 Appendix B

For Euler equations, the classical well-balanced approach assumes that a correct approximation of the main physical patterns will be catched using the one-dimensional system :

$$\left\{ \begin{array}{l} \dfrac{\partial \rho S(x)}{\partial t} + \dfrac{\partial \rho u S(x)}{\partial x} = 0 \\ \dfrac{\partial \rho u S(x)}{\partial t} + \dfrac{\partial \rho u^2 S(x)}{\partial x} + S(x)\dfrac{\partial P}{\partial x} = 0 \\ \dfrac{\partial E S(x)}{\partial t} + \dfrac{\partial u(E+P) S(x)}{\partial x} = 0 \end{array} \right. \tag{23}$$

where S(x) denotes the -steady- transverse section in a pipe, assuming that the x-axis is aligned with the main direction of the flow in the pipe. System (23) is established by a straightforward integration on big control volumes, assuming in practice that the section $S(x)$ is at least C^1. The well-balanced approach consists in adding first an obvious equation $\frac{\partial S(x)}{\partial t} = 0$; then two -left and right- fluxes $F^{\pm}$ are computed on each cell interface, (here the second component $F^+ \neq F^-$ when focusing on the momentum equation), assuming a uniform section $S(x)$ within each cell -thus with a jump on each cell interface-, together with uniform physical states ρ, U, P within each cell, as usual. Thus the Riemann problem that has to be solved at each cell interface at each time step must take non-conservative terms $S(x)\frac{\partial P}{\partial x}$ into account in a suitable way. Actually, the connection of states around the steady wave $\lambda = 0$ is enforced by imposing that the Riemann invariants of the steady wave are preserved on both sides of $x/t = 0$. This makes sense since the associated steady wave is linearly degenerated. For the Euler set of equations described above in system (23), these Riemann invariants I_0^k are simply $I_0^1 = Q = \rho u S(x)$, $I_0^2 = QH$ and the entropy $I_0^3 = \eta(P, \rho)$. For more details on the Well Balanced approach, we refer the reader to references [16,17,19], among others.

10 Bibliography

References

[1] Audebert, B. and Hérard, J.-M. and Martin, X. and Touazi, O., A simple integral approach to compute flows in ducts with variable cross section, *EDF report H-I85-2014-05201-EN*, submitted for publication 2014.

[2] Audusse, E. and Bouchut, F. and Bristeau, M.O. and Klein, R. and Perthame, B., A robust and entropy-satisfying numerical scheme for fluid flows in discontinuous nozzles, *SIAM J. of Sci. Comp.*, pp.2050-2065, vol.25,2004.

[3] Bear, J., Dynamics of fluids in porous media, *Courier Corporation*, 1972.

[4] Berry, R.A. and Peterson, J.W. and Zhang, H. and Martineau, C. and Zhao, H. and Zou, L. and Andrs, A. , RELAP-7. Theory Manual , *INL report INL/EXT-14-31366*, december 2014.

[5] Code-Saturne 4.0. Theory Manual, http://code-saturne.org/cms/sites/default/files/docs/4.0/theory.pdf , *available on http://code-saturne.org/*, 2015.

[6] Coquel, F. and Saleh, K. and Seguin, N., A robust and entropy-satisfying numerical scheme for fluid flows in discontinuous nozzles, *Mathematical Models and Methods in Applied Sciences*, pp.2043-2083, vol.24,2014.

[7] De Ville, A., On the properties of compressible gas flow in a porous media, *Transport Porous Media*, pp.287-306, vol.22,1996.

[8] Dubois F., Boundary conditions and the Osher scheme for the Euler equations of gas dynamics, *CMAP report, Ecole Polytechnique*, 1987.

[9] Eymard, R. and Gallouët, T. and Herbin, R., Finite Volume Methods, *Handbook of Numerical Analysis*, pp.713-1018, 2000.

[10] Eymard, R. and Gallouët, T. and Guichard, C. and Herbin, R. and Masson, R., TP or not TP, that is the question, *Computational Geosciences*, pp. 285-296, vol. 18(3-4) 2014.

[11] Eymard, R. and Gallouët, T. and Herbin, R., Discretization of heterogeneous and anisotropic diffusion problems on general nonconforming meshes SUSHI: a scheme using stabilization and hybrid interfaces, *IMA Journal of Numerical Analysis*, 2009.

[12] Eymard, R. and Henry, G. and Herbin, R. and Hubert, F. and Klofkorn, R. and Manzini, G., 3D benchmark on discretization schemes for anisotropic diffusion problems on general grids, *Proceedings of the 6th International Symposium on Finite Volumes for Complex Applications: FVCA6*, pp.895-930, 2011.

[13] Gallouët, T. and Hérard, J.-M. and Seguin, N., On the use of symetrizing variables for vacuums., *Calcolo*, pp.163-194, vol.40, 2003.

[14] Girault, L. and Hérard, J.-M., A two-fluid hyperbolic model in a porous medium., *ESAIM : Mathematical Modelling and Numerical Analysis*, pp.1319-1348, vol.44, 2010.

[15] Girault, L. and Hérard, J.-M. , Multidimensional computations of a two-fluid hyperbolic model in a porous medium., *International Journal on Finite Volumes*, http://ijfv.episciences.org/, https://hal.archives-ouvertes.fr/hal-01114209v1, pp.1-33, 7, 2010.

[16] Gosse, L., A well-balanced scheme using non-conservative products designed for hyperbolic systems of conservation laws with source terms, *Mathematical Models and Methods in Applied Sciences*, pp.339-365, vol.11, 2001.

[17] Gosse, L. and Leroux, A. Y., Un schéma-équilibre adapté aux lois de conservation scalaires non-homogènes, *Comptes rendus de l'Académie des sciences. Série 1, Mathématique*, pp.543-546, vol.323, 1996.

[18] Grandotto, M. and Obry, P., Calculs des écoulements diphasiques dans les échangeurs par une méthode aux éléments finis, *Revue Européenne des Eléments Finis*, pp.53-74, vol.5, 1996.

[19] Greenberg, J.-M. and Leroux, A.-Y., A well-balanced scheme for the numerical processing of source terms in hyperbolic equations., *SIAM Journal on Numerical Analysis*, 1996, pp.1-16, vol.33.

[20] Hérard, J.-M. , A rough scheme to couple free and porous media, *International Journal on Finite Volumes, http://ijfv.episciences.org/, https://hal.archives-ouvertes.fr/hal-01114212v1*, pp.1-28, 3, 2006.

[21] Hérard, J.-M., Un modele diphasique bifluide en milieu poreux, *Comptes Rendus Mécanique*, pp.650-655, vol.336(8), 2008.

[22] Hérard, J.-M. and Jung, J., An interface condition to compute compressible flows in variable cross section ducts, *in revised form*, 2015.

[23] Herbin, R. and Hubert, F., Benchmark on discretization schemes for anisotropic diffusion problems on general grids, *Proceedings of the 5th International Symposium on Finite Volumes for Complex Applications: FVCA5*, pp.659-692, 2008.

[24] Idel'Cik, I. E., Memento des pertes de charge, *Collection de la Direction des Etudes et Recherches d'Electricite de France, Paris: Eyrolles*, 1969.

[25] Jung, J., Schémas numériques adaptés aux accélérateurs multicoeurs pour les écoulements bifluides, *PhD thesis, Université Strasbourg, https://tel.archives-ouvertes.fr/tel-00876159v2*, 2013.

[26] Kröner, D. and Thanh, M. D. , Numerical solutions to compressible flows in a nozzle with variable cross-section., *SIAM Journal on Numerical Analysis*, 2006, pp.796-824, vol.43.

[27] Le Coq, G. and Aubry, S. and Cahouet, J. and Lequesne, P. and Nicolas, G. and Pastorini, S., The THYC computer code. A finite volume approach for 3 dimensional two-phase flows in tube bundles, *Bulletin de la Direction des études et recherches-Electricité de France. Série A, nucléaire, hydraulique, thermique. In french*, pp.61–76, 1989.

[28] Martin, X. , Numerical modeling of flows in obstructed media , *PhD thesis, Université Aix Marseille*, in preparation.

[29] Rochette, D. and Clain, S., Mathematical model and simulation of gas flow through a porous medium in high breaking capacity fuses, *Heat and Fluid Flow*, pp. 115-126, vol.25,2004.

[30] Rochette, D. and Clain, S. and Buffard, T. , Numerical scheme to complete a compressible gas flow in variable porosity media, *International Journal of Computational Fluid Dynamics*, pp. 299-309, vol.19,2005.

[31] Toumi, I. and Bergeron, A. and Gallo, D. and Royer, E. and Caruge, D., FLICA-4: a three-dimensional two-phase flow computer code with advanced numerical methods for nuclear applications, *Nuclear Engineering and Design*, pp. 139-155, vol.200, 2000.

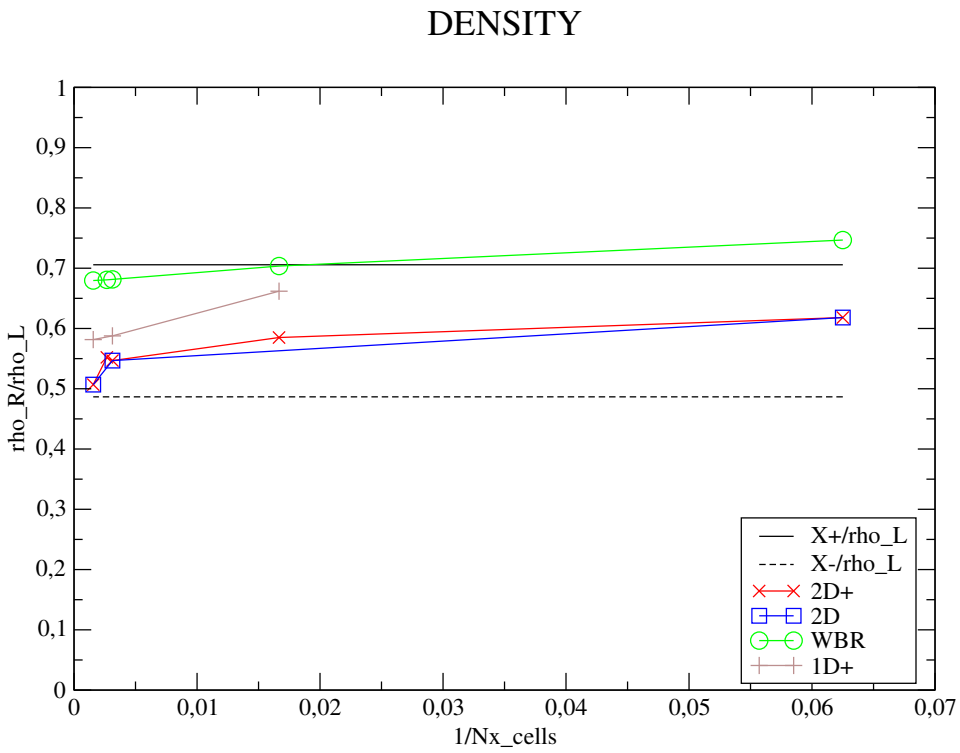

Figure 28: Test case B. Density ratio between the right side and the left side of the contraction, as a function of the mesh size h. The blue squares (resp. red crosses) refer to the full two-dimensional simulation (respectively to the new $2D+$ approach). Computational results are also compared with those provided by the one -dimensional approach, following either the classical porous (or variable cross section) approach, while using the Well-balanced scheme of Kröner and Thanh (green circles), or the integral $1D+$ approach introduced in reference [1] (brown crosses). X^- and X^+ correspond to the density roots of equations (16), (17) and (18) provided in section 4.2. The full black line (resp. dashed black line) corresponds to the ratio of X^+ (resp. X^-) normalized by the given density ρ_L.

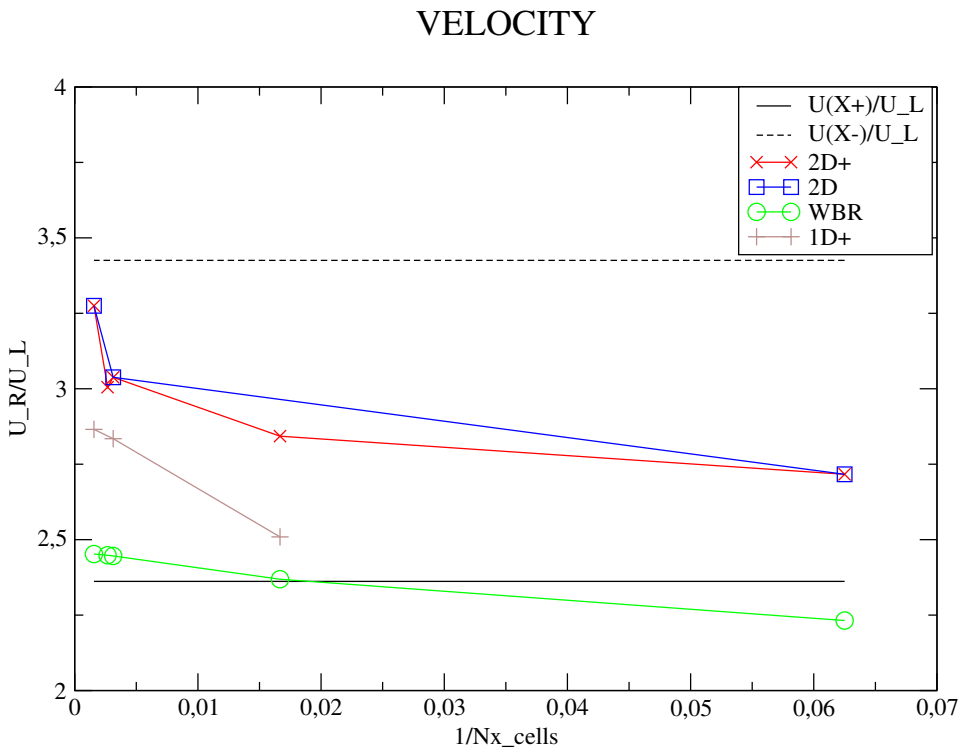

Figure 29: Test case B. Velocity ratio between the right side and the left side of the contraction, as a function of the mesh size h. The blue squares (resp. red crosses) refer to the full two-dimensional simulation (respectively to the new $2D+$ approach). Computational results are also compared with those provided by the one -dimensional approach, following either the classical porous (or variable cross section) approach, while using the Well-balanced scheme of Kröner and Thanh (green circles), or the integral $1D+$ approach introduced in reference [1] (brown crosses). X^- and X^+ correspond to the density roots of equations (16), (17) and (18) provided in section 4.2. The full black line (resp. dashed black line) corresponds to the ratio of the velocity $U(X^+)$ (resp. $U(X^-)$) normalized by the given velocity U_L.

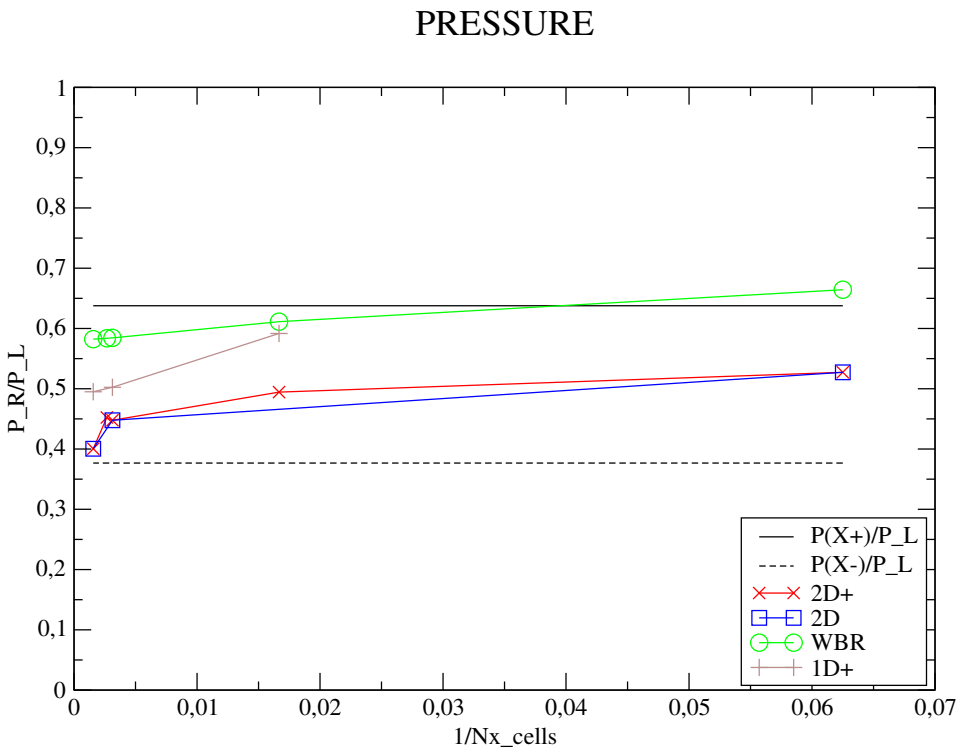

Figure 30: Test case B. Pressure ratio between the right side and the left side of the contraction, as a function of the mesh size h. The blue squares (resp. red crosses) refer to the full two-dimensional simulation (respectively to the new $2D+$ approach). Computational results are also compared with those provided by the one -dimensional approach, following either the classical porous (or variable cross section) approach, while using the Well-balanced scheme of Kröner and Thanh (green circles), or the integral $1D+$ approach introduced in reference [1] (brown crosses). X^- and X^+ correspond to the density roots of equations (16), (17) and (18) provided in section 4.2. The full black line (resp. dashed black line) corresponds to the ratio of the pressure $P(X^+)$ (resp. $P(X^-)$) normalized by the given pressure P_L.

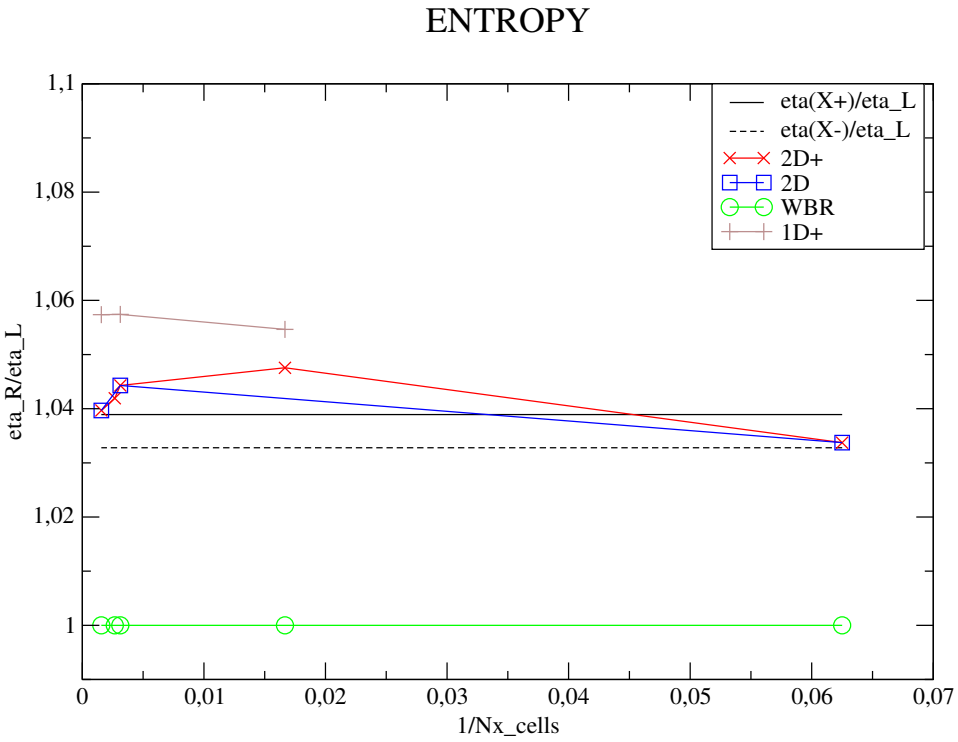

Figure 31: Test case B. Entropy ratio between the right side and the left side of the contraction, as a function of the mesh size h. The blue squares (resp. red crosses) refer to the full two-dimensional simulation (respectively to the new $2D+$ approach). Computational results are also compared with those provided by the one -dimensional approach, following either the classical porous (or variable cross section) approach, while using the Well-balanced scheme of Kröner and Thanh (green circles), or the integral $1D+$ approach introduced in reference [1] (brown crosses). X^- and X^+ correspond to the density roots of equations (16), (17) and (18) provided in section 4.2. The full black line (resp. dashed black line) corresponds to the ratio of the entropy $\eta(X^+)$ (resp. $\eta(X^-)$) normalized by the given entropy η_L.